On the potential of recording earthquakes for global seismic tomography by low-cost autonomous instruments in the oceans

Frederik J. Simons, Guust Nolet, Paul Georgief, Jeff M. Babcock, Lloyd A. Regier, Russ E. Davis

On the potential of recording earthquakes for global seismic tomography by low-cost autonomous instruments in the oceans

Frederik J. Simons,[1] Guust Nolet,[1] Paul Georgief,[2] Jeff M. Babcock,[2]
Lloyd A. Regier,[3] and Russ E. Davis[3]

Received 9 September 2008; revised 14 January 2009; accepted 5 March 2009; published 23 May 2009.

[1] We describe the development and testing of an autonomous device designed to revolutionize Earth structure determination via global seismic tomography by detecting earthquakes at teleseismic distances in the oceans. One prototype MERMAID, short for Mobile Earthquake Recording in Marine Areas by Independent Divers, was constructed and tested at sea. The instrument combines two readily available, relatively low-cost but state-of-the-art components: a Sounding Oceanographic Lagrangian Observer, or SOLO float, and an off-the-shelf hydrophone, with custom-built data logging hardware. We report on the development of efficient wavelet-based algorithms for the detection and discrimination of seismic events and analyze three time series of acoustic pressure collected at a depth of 700 m in pilot experiments conducted offshore San Diego, CA. In these tests, over 120 hours of data were gathered, and five earthquakes, of which one was teleseismic, were recorded and identified. Quantitative estimates based on these results suggest that instruments of the MERMAID type may collect up to a hundred tomographically useful teleseismic events per year. The final design will also incorporate a Global Positioning System receiver, onboard signal processing software optimized for low-power chips, and high-throughput satellite communication equipment for telemetered data transfer. With these improvements, we hope to realize our vision of a global array of autonomous floating sensors for whole-earth seismic tomography.

Citation: Simons, F. J., G. Nolet, P. Georgief, J. M. Babcock, L. A. Regier, and R. E. Davis (2009), On the potential of recording earthquakes for global seismic tomography by low-cost autonomous instruments in the oceans, *J. Geophys. Res.*, *114*, B05307, doi:10.1029/2008JB006088.

1. Introduction and Motivation

[2] Despite the rapid advances in determining the three-dimensional seismic wave speed, density and attenuation structure of the Earth that were made in the 1980s and 1990s [*Romanowicz*, 1991, 2003], progress in seismic tomography has now slowed due to lack of global earthquake data from oceanic stations. This severely hampers our ability to image large sections of the mantle. Sampling is poorest in the southern hemisphere where a number of mantle plumes, including two superplumes beneath the Pacific and African plates, likely play a large role in driving the Earth's heat engine.

[3] While normal-mode [e.g., *Ishii and Tromp*, 1999] finite-frequency [e.g., *Dahlen et al.*, 2000], and noise-correlation analyses [e.g., *Campillo and Paul*, 2003] mitigate the sampling problem to some extent, whole-Earth imaging remains data limited. The most straightforward route to enhanced model resolution and the exploration of the Earth's uncharted interior is through increasing the number of seismic stations where they are scarcest: in the oceans. Of the roughly 200 digital broadband stations with real-time data availability that currently fall under the umbrella of the International Federation of Digital Seismograph Networks (FDSN, www.fdsn.org), the vast majority are located on continents. This leaves only scattered station coverage, mostly on ocean islands, over the remaining two thirds of the Earth's surface [*Romanowicz and Giardini*, 2001; *Romanowicz*, 2008].

[4] In addition to isolated island stations, most broadband seismic data suitable to improve global tomographic Earth models is collected by ocean bottom seismometers (OBS [*Bradner*, 1964; *Stephen et al.*, 2003]). These need to be sunk to the ocean bottom from a research vessel and are usually recovered for data collection, which, owing to the cost of ship time, is very expensive. Recovery remains technically challenging, even if failed retrievals sometimes are remarkable discoveries by themselves [*Tolstoy et al.*, 2006]. Notwithstanding certain impressive scientific successes [e.g., *Zhao et al.*, 1997; *Forsyth and the Melt Seismic Team*, 1998; *Smith et al.*, 2001; *Isse et al.*, 2004; *Tibi et al.*,

[1]Geosciences Department, Princeton University, Princeton, New Jersey, USA.
[2]Institute of Geophysics and Planetary Physics, Ocean Bottom Seismometry Laboratory, Scripps Institution of Oceanography, La Jolla, California, USA.
[3]Physical Oceanography Research Division, Instrument Development Group, Scripps Institution of Oceanography, La Jolla, California, USA.

0148-0227/09/2008JB006088$09.00

2006; *Laske et al.*, 2007] the use of OBS is prohibitively expensive for the dense coverage required for global tomography of the southern hemisphere.

[5] Among the latest solutions proposed is the installation of ocean-bottom seismometers in the deep oceans connected to shore via abandoned telephone cables or visited by robotic underwater vehicles [*Duennebier et al.*, 2002; *Romanowicz et al.*, 2006]. The first seismic station connected to a phone cable (station H2O) has been abandoned due to funding shortfalls after technical difficulties. The second option was considered at the ORION (Ocean Research Interactive Observatory Networks) workshop in San Juan, PR, in 2004, but no perspective for sustained funding is in sight. With both technical and financial problems it is difficult to see how these efforts can provide sufficient instrument coverage on the ocean floor in the near term.

[6] Seismic data collection in the ocean need not be limited to instruments buried in the ocean floor. Indeed, (anchored) sonobuoys [*Reid et al.*, 1973; *Bradner and Brune*, 1974; *Kebe*, 1981; *Cotaras et al.*, 1988] and moored hydrophones [*Fox et al.*, 1993; *Slack et al.*, 1999; *Fox et al.*, 2001; *Bohnenstiehl et al.*, 2002; *Butler and Lomnitz*, 2002; *Smith et al.*, 2002, 2004; *Dziak et al.*, 2004; *de Groot-Hedlin*, 2005] have shown potential to record earthquakes but have not generally been able to give an acceptable signal-to-noise ratio for all but the closest or strongest events. High installation and recovery costs disqualify moored instruments, in our opinion, as lasting solutions to the seismic coverage gap.

[7] Neutrally buoyant freely drifting "Lagrangian" devices provide a potentially cost-effective alternative. *Bradner et al.* [1970] were the first to suggest using "Swallow" floats [*Swallow*, 1955] for seismometry. Similar ideas were further developed by *Hodgkiss and Anderson* [1983] and *D'Spain et al.* [1991]. The advantages of "divers" or "floats" for seismic data acquisition are their relatively low manufacturing cost, avoidance of vibration and flow noise [*Webb*, 1988; *D'Spain et al.*, 1991], and small size and weight allowing their deployment from a wide range of platforms [*Dalton*, 2002]. The advent of "profiling" floats [*Davis et al.*, 1992] which can repeatedly cycle to a specified target pressure and resurface to transmit data collected in near-real time led to the idea of long-lived oceanic seismic monitoring arrays. The inevitable sacrifices are that they only record pressure phases; they suffer from geographical location uncertainty that depends on their rise speed and the prevailing current conditions at surfacing; and they are severely power limited owing to the usually nonrenewable battery charge, although alternative energy sources are being proposed [*Webb et al.*, 2001; *D'Asaro*, 2007].

[8] In this paper we report on the development and initial testing of a new kind of instrument, nicknamed MERMAID (Mobile Earthquake Recording in Marine Areas by Independent Divers). Our prototype is based on the Sounding Oceanographic Lagrangian Observer (SOLO) by *Davis et al.* [2001] to which we fitted an off-the-shelf hydrophone and a custom recording package. The ultimate goal is a MERMAID-type instrument, which will be completely autonomous and perform all the necessary operations on board and at depth, to detect, discriminate and identify the teleseismic events that are of most utility in large-scale Earth structure determinations. These operations will be carried out in the time domain and in the wavelet domain. Analog Short-Term/Long-Term Averaging (STA/LTA) detection will wake up a digital analysis system for additional processing of the recorded signal through a fast discrete wavelet transform. Positive identifications will be sent as waveforms via satellite (e.g., IRIDIUM). To date, our prototype only comes equipped with a large recording buffer and a Telonics ARGOS uplink transmitter. We collected data in situ but the real-time data detection and transmission have not yet been tested. Our test deployments were recovered, however in its final design, MERMAID will collect and analyze data at depth, surfacing for GPS position determination and communication, and repeating this cycle until the batteries are depleted.

[9] In this paper we focus first on signal processing, with special attention to the expected power limitation of instruments based on our prototype. Training data from moored hydrophones [*Fox et al.*, 2001] is used to inform the analysis of over 120 hours of MERMAID data collected at a depth of about 700 dbar (roughly the equivalent in m) offshore San Diego, CA. We describe the deployment and recovery operations accomplished using the research vessel "Saikhon" during three field tests in November 2003, September 2004, and August 2007. These experiments returned several positive earthquake identifications, and one of these was of sufficient magnitude (M_w 6.0) and epicentral distance ($\Delta = 46.5°$) to prove the potential of our prototype ultimately improving seismic coverage in the oceans [*Simons et al.*, 2006b]. Altogether our results allow us to estimate the likely numbers of useful events detectable by a single instrument during longer-term campaigns at up to 100 per year.

2. MERMAID Prototype

[10] Figure 1 shows the MERMAID prototype as it was used for the field tests. An aluminum casing contains a dual pump-and-bladder system that allows the instrument to achieve neutral buoyancy between the surface and about 2000 m depth, depending on the local density profile of the ocean [*Davis et al.*, 2001]. The cut-away plan illustrates the seismological modifications to this otherwise standard-issue SOLO float. A High Tech HTI-90-U hydrophone was mounted on the outside and connected to the seismic recording package located inside the top screw cap. The recording unit contains a second clock in addition to the instrument clock, filters, an A/D converter and a flash memory card. The data sampling rate was set to 20 Hz, and the data were recorded with 16 bit precision. The data logging equipment was custom built, and modifications between the three pilot deployments caused the instrument characteristics to vary somewhat between experiments. However, the basic properties of the system, including the 16 bit, 20 Hz sampling are not expected to vary in the future. The ARGOS antenna circuitry is located below the screw cap. As ARGOS permits only low-volume data transmission (in the low kB range per message), planned additions include an IRIDIUM satellite transfer protocol and a Global Positioning System (GPS) receiver.

[11] The instrument is about 1.50 m long and weighs around 25 kg. It is thus suitable for manual deployment by

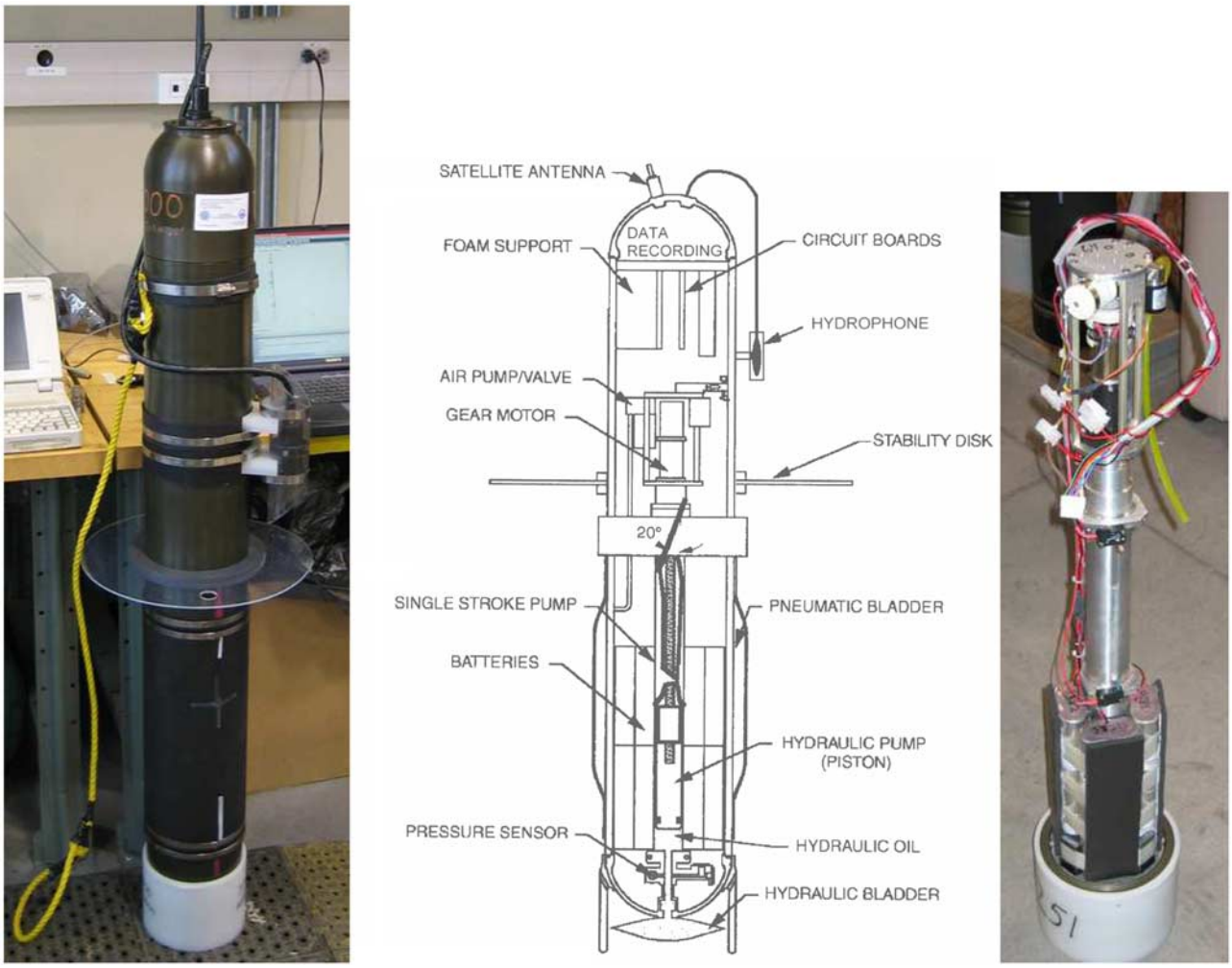

Figure 1. The MERMAID prototype: a SOLO float equipped with an externally mounted hydrophone and a recording and processing unit. (left) Outside view. (middle) Design schematic. (right) The interior rise-and-dive mechanism, cabling, and lithium battery packs.

untrained personnel from any vessel or aircraft. The three test deployments, scenes of which are depicted in Figure 2, were conducted from the Mission Bay marina outside San Diego, CA. The instrument was carried by the 27 ft research vessel "Saikhon" to its oceanic dive locations of 32°55.005′N 117°37.822′W in November 2003, 32°55.038′N 117°37.848′W in September 2004, and 32°52.359′N 117°39.026′W in August 2007. The recovery after resurfacing was facilitated by the ARGOS position fixes and aided by a radio direction finder.

[12] Figure 3 shows the raw data collected during the course of the three pilot experiments. Over 39 h of data were collected in November 2003, about 37 h in September 2004, and over 45 h in August 2007. While sea conditions were similar during the three deployments, the time series shown differ in character due to hardware adjustments between experiments. MERMAID reached a depth of ~705 dbar in under 5 h. At preprogrammed times the instrument pump was reactivated twice with an interval of 1 h in order to adjust and maintain its target depth. Each of the pump runs last about 200 s; they are marked by gray vertical bars in the time series. The mechanically quiet periods after pumping are only disturbed by the prevailing ocean "noise," including any seismic activity. After the drift period at depth, the pump was turned on once again and the instrument reached the surface about 1 h later.

[13] The location of the instrument at the time of recording the incoming seismic wavefield must be determined precisely; a timing error below 0.1 s is desirable for global tomography [*Nolet*, 2008]. Owing to weight and power limitations, incorporating a full-ocean depth fathometer is ruled out as an opion. Given a typical rising velocity of under 20 cm s^{-1} [*Davis et al.*, 2001], the current speeds between the surface and the cruising depth are the main uncontrollable variables. These are now also increasingly being mapped with SOLO floats and are frequently around 10–20 cm s^{-1} worldwide [*Park et al.*, 2004; *Davis*, 2005; *Willis and Fu*, 2008; *Xie and Zhu*, 2008]. The time required to get a position fix after surfacing using GPS (unlike ARGOS) is within minutes. During our 2–3 day pilot experiments at 700 m depth offshore San Diego, CA, the mean drift was less than 5 cm s^{-1}. With a position uncertainty on the order of 1–2 km when parked above 1000 m depth, it is thus possible in principle for MERMAID to collect tomog-

Figure 2. Scenes from the MERMAID deployments in the waters offshore San Diego, CA. (top) Transportation to and from the deployment location by truck and boat. The secondary bladder, a rubber sleeve filled with air, is seen in a semi-inflated condition. (bottom left) Close-up of the side-mounted hydrophone. (bottom right) Surfacing between dives, with the ARGOS satellite antenna emerging.

raphy quality traveltimes. Noise levels for acoustic pressure recorded in the band near 1 Hz, where we expect useful teleseismic arrivals, scale with prevailing wind speeds [*McCreery and Duennebier*, 1993; *Babcock et al.*, 1994; *Wilcock et al.*, 1999]. In our experiments, significant wave heights most likely did not surpass 1.5–2 m (cdip.ucsd.edu) and wind speeds were generally low. These relatively quiet [*Bauer and Staabs*, 1998] experimental conditions caution against an overly optimistic interpretation of the results presented in this paper.

[14] The scientific analysis of undifferentiated time series as in Figure 3, will ultimately be the task of the low-power processing unit onboard. In order to train the instrument to reliably detect and discriminate seismic signals, we investigated several approaches. Some general considerations are discussed in section 3 and the analysis of training data will be presented in section 4. Examples of positive seismic detections from the recorded time series will be shown in section 5.

3. Detecting and Discriminating Seismic Signals

3.1. Time-Domain Techniques

[15] The detection and discrimination of seismic signals by terrestrial seismometers, and the transmission of the results by (satellite) telemetry [e.g., *Poupinet et al.*, 1989] dates back to the early nineteen seventies, when the age of digital seismometry began. The workhorse remains the Short-Term/Long-Term Averaging (STA/LTA) algorithm [e.g., *Allen*, 1978], which typically triggers on the ratio of the average absolute value (in two time windows of unequal length) of the detrended and possibly prefiltered traces. This procedure is suitable both for analog and digital implementation, the former drawing less power.

[16] Local earthquakes [*Allen and Kanamori*, 2003], regional earthquakes [*Gledhill*, 1985] and teleseismic earthquakes [*Evans and Allen*, 1983] all necessitate their own parameter settings. Moreover, these algorithms are based on negative decision logic that detects all deviations from the ambient noise but also includes many false alarms [*Joswig*, 1990]. As false alarms lead to power-draining surfacing and data transmission, we will use STA/LTA for first-cut analysis only.

3.2. Time-Frequency and Frequency-Domain Analysis

[17] Approaches based upon criteria that test for positive correlation with known signal patterns (very broadly speaking, "pattern recognition" [*Joswig*, 1990]) circumvent the above mentioned problems with time domain triggering techniques. Here too, the subject has some history in seismology. Short-time sequency-domain (using Walsh basis functions) techniques [e.g., *Goforth and Herrin*, 1981], or short-time frequency domain (Fourier expansion) techniques [e.g., *Gledhill*, 1985] have been proposed and used at various times. It is important to note the distinction and the difference in relative requirements between detection and accurate timing. Frequency- (and sequency-) domain techniques are more sensitive in the detection but worse at achieving timing accuracy [*Allen*, 1982]. In addition, computation speed and numerical complexity have to be taken into account. In general, frequency domain techniques are too slow, except on dedicated chips [*Gledhill*, 1985]. Walsh function approaches may be more efficient, as they require logical comparisons, not arithmetic ones.

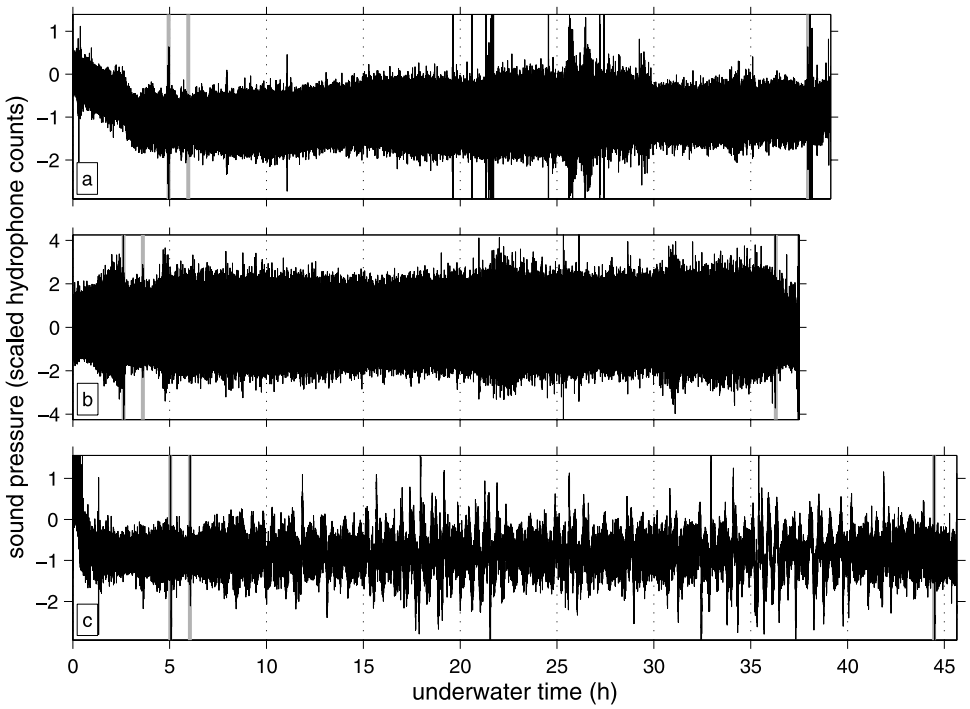

Figure 3. Uncorrected raw pressure data collected during the immersed periods of the (a) November 2003, (b) September 2004, and (c) August 2007 recovered deployments of the MERMAID prototype float. Electronic and acoustic settings varied between experiments. The graph ordinates are in arbitrary hydrophone units, scaled, clipped, and offset to an average of 0 in the first 15 minutes of each experiment; zeroes on the time axis correspond to the times of immersion. All times shown here in hours (h) are approximate using the nominal 20-Hz sampling rate. The temporal bias from clock drift was corrected before the analysis. Approximate times of pump activity are indicated by thick gray vertical lines. The long central portions of the records are free of any mechanical activity and reflect sound pressure variations at the drifting depths of 705 ± 5 dbar.

[18] The central problem with any transform of this sort is redundancy. A sequence of N numbers is segmented into X overlapping sections prior to (Fourier) transformation on an equally spaced grid of Y frequencies. The resulting windowed spectral representation of the signal comprises $X \times Y > N$ samples of the time-varying spectral density (the "spectrogram"), and it is not invertible.

[19] Together, time-domain and time-frequency analysis usually reveal much diagnostic information that can readily be interpreted by the human eye and cast into automated algorithms, to study (or remove) all kinds of nonseismic sources, from noise on land by vehicles (cars, trucks, trains), to waterfalls and waves in local bodies of water, to sonic booms [*Evans and Allen*, 1983], animals [*O'Hanlon*, 2001], wind gusts [*Gledhill*, 1985], telephone lines [*Allen*, 1982], or large marine mammals [*Nishimura and Conlon*, 1993]. However, for the reasons mentioned above, calculating and analyzing the spectrogram is not a particularly efficient way of utilizing the limited power available on an oceanic float. We will, however, use it for both human and machine training and learning purposes.

[20] Finally, we will calculate the power spectral density of the signal, which provides a measure of the frequency-dependent energy of the signal across the entire analysis window, using the Welch Overlapping Segment Analysis (WOSA) with a single Slepian data taper [*Percival and Walden*, 1993] and the robust algorithm developed by *Chave et al.* [1987]. This enables comparisons with published models of ocean noise [e.g., *Wenz*, 1962; *Webb and Cox*, 1986; *Cox and Jacobs*, 1989; *D'Spain et al.*, 1991; *Babcock et al.*, 1994; *Webb*, 1998].

3.3. Wavelet Analysis

[21] As explained above, "time frequency" implies "redundancy": the short-time Fourier transform does not form an orthogonal basis [*Daubechies*, 1992; *Mallat*, 1998]. Fortunately, more efficient and nonredundant signal representations can be achieved by the wavelet transform [e.g., *Rioul and Vetterli*, 1991; *Kumar and Foufoula-Georgiou*, 1997]. Certain authors have reported success in using wavelet-based treatments for the problem of seismic signal representation [e.g., *Chakraborty and Okaya*, 1995], detection [*Simons et al.*, 2006a], and type discrimination, which is relevant for our purpose [e.g., *Gendron et al.*, 2000].

[22] In our proposed design, once MERMAID's digital systems are activated for analysis of promising segments by the analog STA/LTA triggering algorithm, the relevant data buffer will be wavelet transformed, and informed by prior training data, the scalogram (the time-varying pattern of the magnitude of the wavelet coefficients) will be the basis of the decision to surface and transmit or not.

[23] The discrete wavelet transform is nonredundant. Instead of estimating the amplitudes belonging to certain frequencies at certain times, as in the time-frequency

spectrogram, the discrete wavelet transform isolates time-dependent contributions to the waveform on the basis of coarseness or scale. It does this on a dyadic grid, with the timescale plane tiled so that coarse scales are sampled in the time domain at half the rate of the next finer scale. As a result, the wavelet transform generates exactly as many scale-dependent coefficients as there are samples in the seismogram.

[24] There are numerous wavelet bases [*Daubechies*, 1990; *Mallat*, 1998] and algorithms [*Strang and Nguyen*, 1997; *Jensen and la Cour-Harbo*, 2001]. We use a biorthogonal construction [*Cohen et al.*, 1992] with two and four vanishing moments for the primal and dual wavelets respectively, and abbreviate this as the CDF (2,4) construction. We use the fast "lifting" algorithm [*Sweldens*, 1996]. Besides boasting a computation speed that is asymptotically (as the number of vanishing moments increases) twice as fast as the polyphase algorithm [*Strang and Nguyen*, 1997; *Jensen and la Cour-Harbo*, 2001; *Daubechies and Sweldens*, 1998], the lifting scheme has two added advantages. Firstly, the coefficients can be computed in place without extra memory allocation, and secondly, intermediate operations can be rounded to allow for integer-to-integer transformations [*Calderbank et al.*, 1998]. These properties will be mission-critical, ensuring that MERMAID will need only a small fixed buffer to record limited-precision (e.g., 16 bit) data and to compute the wavelet transform on a very low-power processing unit.

[25] The simplicity of the algorithms for the forward as well as the inverse CDF (2,4) transforms is both intuitively and practically appealing [*Simons et al.*, 2006a]. The signal is subjected to a few iterations of an algorithm that halves the number of samples processed at every step, effectively rearranging the time domain samples to coefficients ordered on a scale from coarse to fine.

[26] Arranged in the so-called Mallat multiresolution ordering, the result of the wavelet transform of an input data vector x of length N, where N is a power of two, is contained in the same-length vector x, where the coarsest-scale scaling coefficients, at the fifth scale, comprise the first $N/(2^5)$ entries. This represents the least detailed level of approximation into which the signal is broken down. The wavelet coefficients contain the details missing from the scaling coefficients at decreasing levels of coarseness, at the scales 5, 4, 3, 2 and 1. Those are vectors of length $N/(2^5)$, $N/(2^4)$, $N/(2^3)$, $N/(2^2)$, and $N/(2^1)$. The total signal length is preserved. The lifting algorithm does not require the signal to have a number of samples that is a power of two, although this is more convenient.

[27] A last useful attribute of the wavelet transform is that, via a procedure called wavelet shrinkage, low-magnitude, statistically insignificant, wavelet coefficients can be thresholded or "softly" reduced to zero [*Johnstone and Silverman*, 1997; *Donoho and Johnstone*, 1994]. We have previously adopted this approach with a scale-dependent threshold [*Simons et al.*, 2006a]. In the examples shown here we shall in contrast define one threshold for all resolution levels and replace the original coefficients by their signed distance from it, thus decreasing by a value equal to the threshold, the amplitude of all coefficients that are above it [*Mallat*, 1998]. The zeroing of insignificant wavelet coefficients results in a denoised, compressed representation of the signal. In principle, the transmission of the thresholded wavelet coefficients rather than the original recorded data could save bandwidth, but at this stage in the development it is not clear whether such a reduction is necessary or desirable. Some information would inevitably be lost, and there may be other ways of compressing the data. Nevertheless, the inspection of seismic waveforms reconstructed from thresholded wavelet coefficients is very instructive, as we shall see.

4. Training Data From Moored Hydrophones

[28] In order to analyze the likely noise sources encountered by a free-floating device of the MERMAID type we use actual data collected by hydrophones moored in the axis of the Sound Fixing And Ranging (SOFAR) channel, disregarding possible strumming noise from their tether [*Kebe*, 1981]. This is the closest we can get to simulating data collected in situ. We take data obtained from long-term hydroacoustic monitoring by the EPR [*Fox et al.*, 2001] and MAR [*Smith et al.*, 2004] arrays. The EPR array (1999–2002) of six hydrophones straddled the East Pacific Rise across the Pacific, Cocos and Nazca plates between 10°S and 10°N. The MAR array (1999–2004) of six hydrophones was situated on the flanks of the northern Mid-Atlantic Ridge between the latitudes 15°N and 35°N.

[29] Figure 4 shows six representative "noises" collected by these hydrophones. Analysis methods are ordered by column. In the first column, we show the raw, uncorrected sound pressure levels in the time domain, in arbitrary units scaled for clarity. Subsequent columns show their time-frequency (spectrogram), wavelet (scalogram) and frequency (power spectrum) representations, each based upon the unscaled data. From top to bottom, these are due to ships (Figure 4a), air gun exploration campaigns (Figure 4b), T phases (Figure 4c), as well as vocalizations from blue (*Balaenoptera musculus*, Figure 4d), minke (*Balaenoptera acutorostrata*, Figure 4e) and finback (*Balaenoptera physalus*, Figure 4f) whales [*Nishimura and Colon*, 1993; *McDonald and Hildebrand*, 1995; *Stafford et al.*, 2001]. Seismic T phases [*Tolstoy and Ewing*, 1950] remain an important subject of study in marine seismology [e.g., *Bohnenstiehl et al.*, 2002; *Dziak et al.*, 2004] but as their energy propagates mostly in the water column they are generally unsuitable for global tomography. Thus we consider them as "noise" for our purposes.

[30] All these potential acoustic contaminants appear readily distinguishable from each other in the time domain, but it is to be noted that all of them will trigger STA/LTA algorithms, and that time-domain identification will be inefficient due to the relatively large data volumes involved. Equally inefficient for automatic onboard discrimination (owing to the complexity of the transforms and the redundancy discussed in section 3), but no less diagnostic, are their (time)-frequency representations. We note that areas of very low power may be due to insensitivity of the hydrophones used or to prior filtering of the records. This is readily apparent from the cool colors in the second column of Figure 4, and most relevant for the study of the T phase, whose power is not expected to be as low as shown in the 0–5 Hz infrasound range [*Dziak et al.*, 2004]. Ship noise is distinguished by harmonic horizontal lines in the spectro-

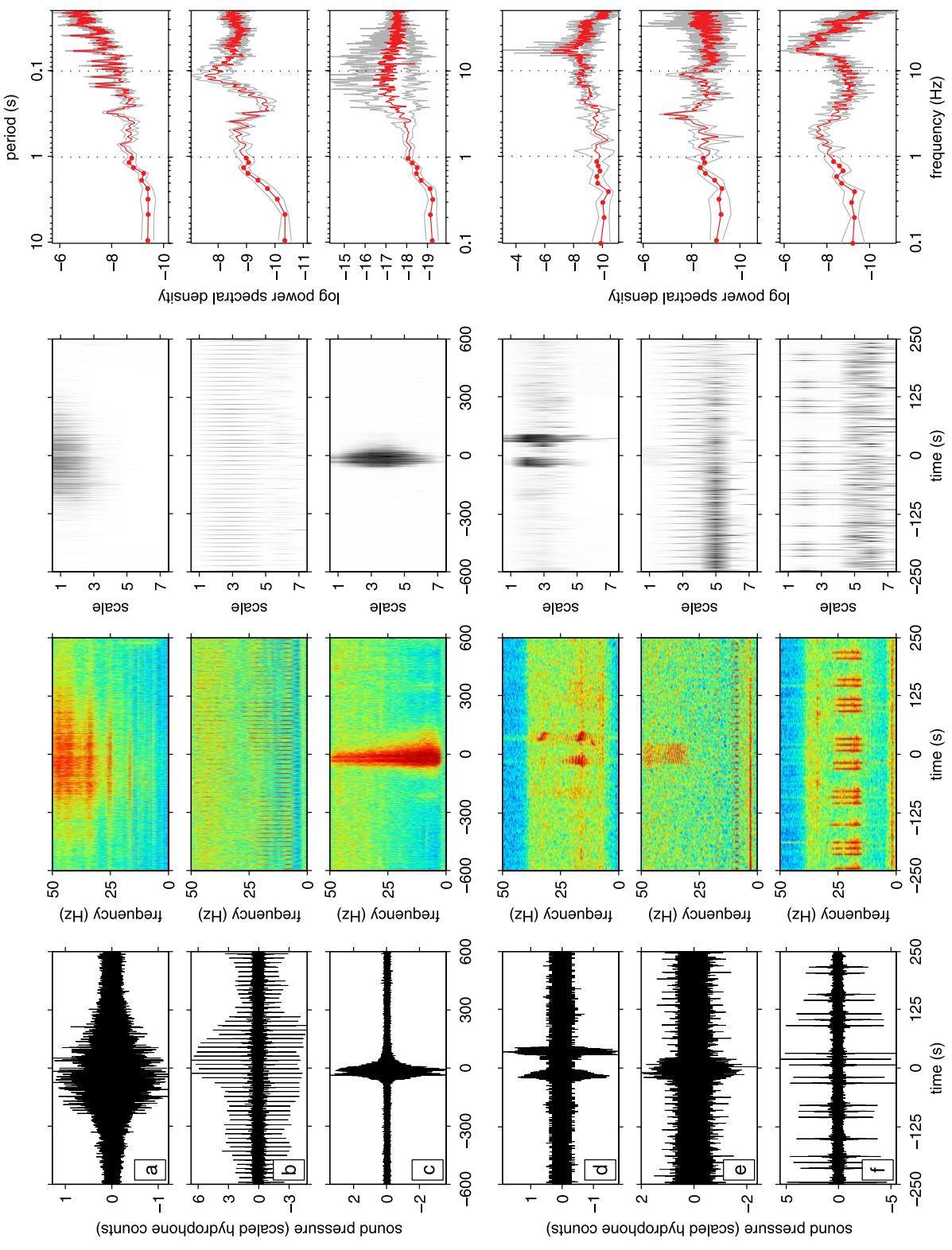
sound pressure (scaled hydrophone counts)
time (s)
frequency (Hz)
scale
log power spectral density
period (s)
frequency (Hz)
log spectral density (stdev from mean)
wavelet coeff magnitude (stdev)
a
b
c
d
e
f

Figure 4

gram or vertical peaks in the power spectrum [*Gray and Greeley*, 1980]. The time-domain peaks of air gun shots are apparent as vertical lines with power at all frequencies in the spectrogram, and generally elevated levels of power at all frequencies in the power spectrum. The emergent, high-frequency *T* phases lack a clear onset and show a preferential frequency decay with time. Finally, the spectral signature of whale song is unmistakable upon detailed analysis of the spectrogram.

[31] Due to the generally higher-frequency content of the nonseismic noise sources, it is possible to remove them through simple (analog) filtering or lowering the sampling rate, as teleseismic arrivals are not expected to contain much power at frequencies above a few Hz [*Aki*, 1967; *Webb*, 1998; *Dziak et al.*, 2004] To analyze the removal of the effects of *T* phases, and for completeness, however, Figure 4 also shows the wavelet-based (thresholded) scalograms of all such noises. The clearest signature is indeed due to the *T* phase, with much power arriving at all scales, allowing for the lack of power of the highest, thus coarsest, scale, which is presumably due to the low-frequency roll-off in hydrophone sensitivity.

5. Analysis of MERMAID Data

[32] The ultimate free-floating instrument is capable of detecting and discriminating teleseismic events autonomously onboard. In order to achieve this goal we needed basic familiarity with potential noise sources, which we obtained from similar instruments as detailed in section 4. However, to train MERMAID to allow for positive recognition, we studied the presence or absence of known seismic arrivals in the record sections.

[33] The United States Geological Survey NEIC seismic catalog reported 389 events in total whose pressure conversions we predicted to arrive during one of our recording experiments. As earthquake statistics would have it, these ranged across local, body wave and moment magnitudes between 1 and 6. A magnitude 6.6 earthquake occurred at an epicentral distance of about 87° while the instrument was recording at the surface on 6 November 2003; predictably (because of the zero-pressure boundary condition) it was not identifiable in the records. All subsequent analysis is focused on the submerged portions of the three experiments, with the time series shown in Figure 3.

[34] Figure 5 shows all of the earthquakes recorded so far by MERMAID, in the same layout as Figure 4. With prior knowledge as to what was being detected, the time domain seismograms are presented after bandpass filtering within the ranges shown in the top left of the panels of the first column. Also noted are the event magnitude, depth, and epicentral distance to the last known instrument location (thus not corrected for the underwater drift). With respect to this same location, the arrival times of the primary *P* wave were calculated in the *iasp91* model, and the traces were aligned on them. Owing to the unfortunate absence of calibration curves (especially in the low-frequency range below 2 Hz), the pressure scale must remain arbitrary. As in Figure 4 the sound pressure units in the first column were scaled for visual clarity, but the power spectral densities in the last column are reported without scaling.

[35] From the point of view of global tomography, the event shown in the first row of Figure 5a is promising [*Simons et al.*, 2006b]. It is of an appreciable moment magnitude (6) and was recorded at a reasonably teleseismic distance (46.5°). This normal-fault earthquake, 110503B in the www.globalcmt.org database, occurred on 5 November 2003 at 5.14°N 77.81°W at a depth of 27.6 km near the west coast of Colombia; its body-wave magnitude was 5.7. The other events, Figures 5b–5e, were of too low magnitude to be of much immediate use in Earth structure determination, but they are included for comparison, and to aid in the analysis of our instrument's overall sensitivity (to follow in section 6). In the time domain, and after filtering, all the events shown present clearly identifiable anomalies of energy which were detected by the STA/LTA algorithm. As spectrograms, shown in the second column, the difference between the large event and the smaller ones is very clear, except for the magnitude 2.8 event at 2.2° (Figure 5d), which eluded attempts at automatic detection based on its time-frequency behavior. The time-frequency signature of the large event is faint, but increased power in the 0–1 Hz range unmistakably identified it. In general, though, this frequency band, where most of the teleseismic energy is expected, contained the most noise in our data set.

[36] After STA/LTA detection of promising time intervals, event discrimination will be based on their wavelet decomposition, i.e. via the scalograms shown in the third column of Figure 5. Based on the training data and using the known seismic events as positive targets, we completed a simple algorithm that searches for increased wavelet power at the largest (coarsest) scale in a small interval after the triggering point, and verifies the absence of such power in most of the scale space above. In testing, our algorithm

Figure 4. Oceanic "noise" recorded by tethered hydrophones not connected with the MERMAID effort; data provided by NOAA/PMEL. (a) Ship noise. (b) Air gun shots. (c) A seismic *T* phase, unsuitable for Earth imaging by global tomography. (d) Blue whale call. (e) A minke whale call. (f) Finback whale calls. The analysis is as follows. (first column) Time domain sections containing (a–c) 1200 s and (d–f) 500 s, respectively, of unfiltered, uncorrected acoustic pressure variations in arbitrarily scaled hydrophone counts. (second column) Spectrograms of the data to the left, calculated using Welch's Overlapping Segment Analysis (WOSA) with 5 s Hann tapers with 87.5% overlap. The time-variable logarithmic spectral density (in units^2/Hz) is shown as the number of standard deviations about the mean of this quantity over the data segment. (third column) Scalograms of the data in the first column: the time variation of the soft-thresholded magnitude of the wavelet coefficients under the biorthogonal (2,4) Cohen-Daubechies-Feauveau (CDF) transform calculated using the lifting scheme. Values are scaled by the standard deviation of this quantity over the segment shown. (fourth column) Logarithmic spectral density (in units^2/Hz) of the raw unscaled data calculated by WOSA on 70% overlapping segments of 250 s length. One prolate-spheroidal taper with a time-bandwidth product $NW = 4$ was used per segment. Chave's method provided robust estimates (red curves with filled red circles to indicate frequency resolution in the low-frequency portion) and jackknifed error estimates showing the 95% confidence intervals (gray curves).

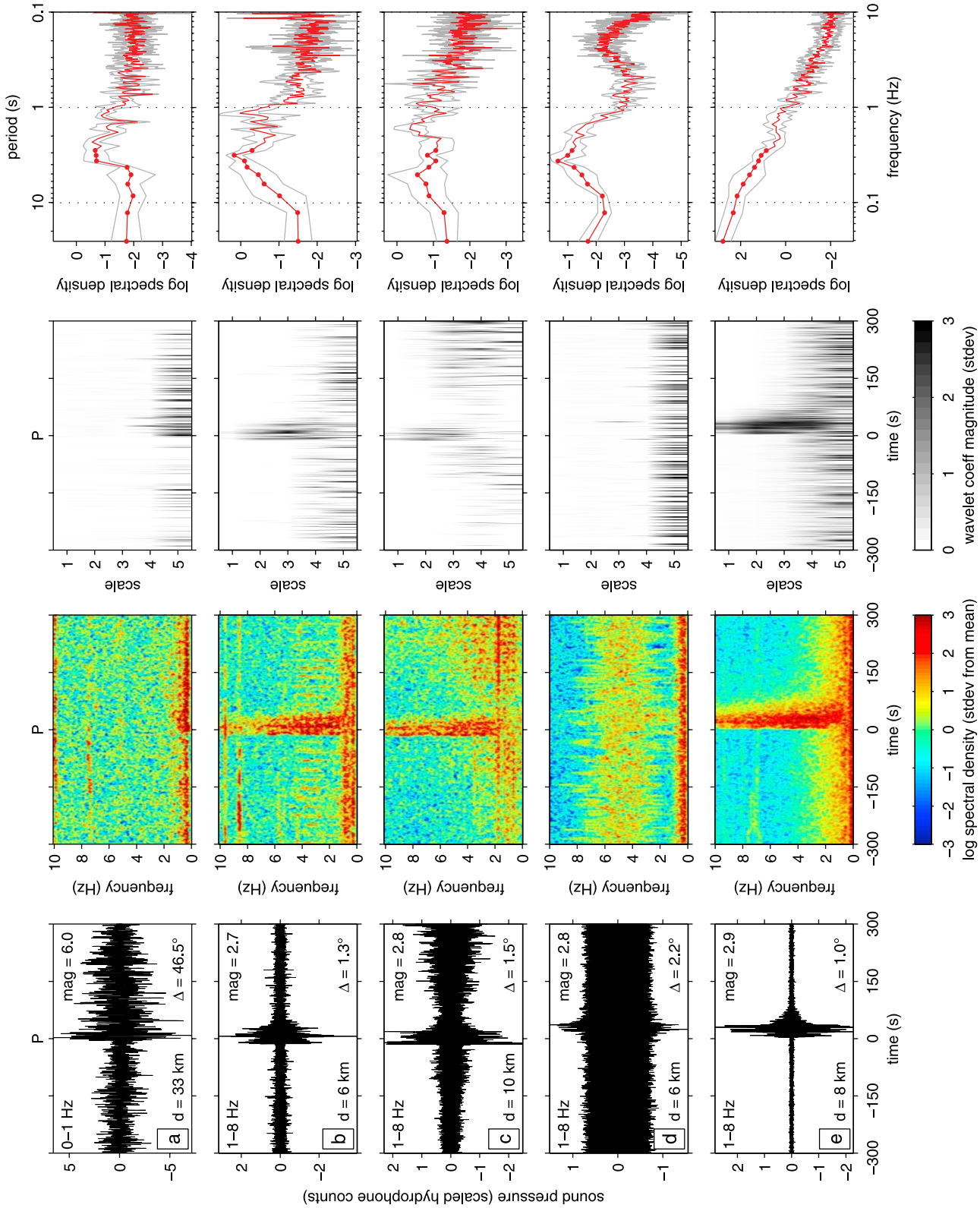
sound pressure (scaled hydrophone counts)
0–1 Hz
1–8 Hz
mag = 6.0
mag = 2.7
mag = 2.8
mag = 2.8
mag = 2.9
Δ = 46.5°
Δ = 1.3°
Δ = 1.5°
Δ = 2.2°
Δ = 1.0°
d = 33 km
d = 6 km
d = 10 km
d = 6 km
d = 8 km
a
b
c
d
e
P
time (s)
frequency (Hz)
scale
log spectral density
period (s)
frequency (Hz)
log spectral density (stdev from mean)
wavelet coeff magnitude (stdev)

Figure 5

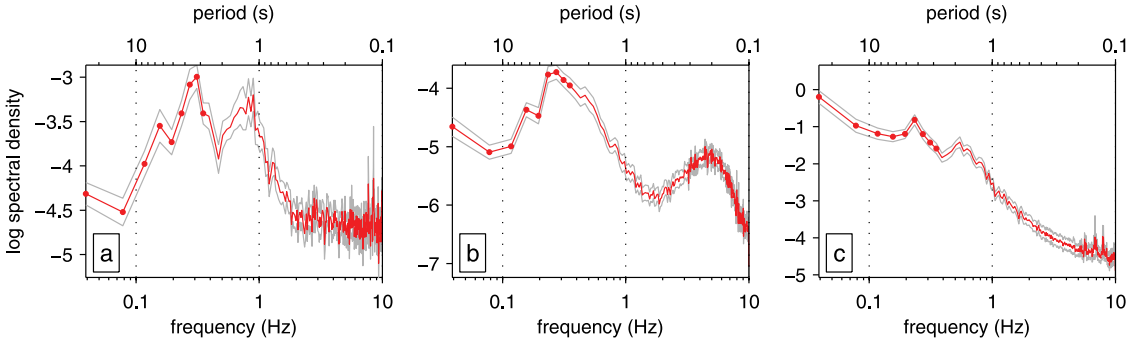

Figure 6. Power spectral density of noise collected at 700 m depth offshore San Diego, CA, during the recovered deployments of the MERMAID prototype float. Plots are labeled to refer to the (a) November 2003, (b) September 2004, and (c) August 2007 experiments, for which raw data were shown in Figure 3 and detected seismic events in Figure 5. To obtain the spectra, the data shown in Figure 3 were divided into hour-long segments, overlapping by 10 minutes. Segments with known mechanical (the pump sequences marked by gray bars in Figure 3) or suspected seismic activity (from detailed examination of their individual power spectral densities) were removed from the analysis, yielding 28, 25, and 38 hour-long segments for the three respective deployments. These were detrended and tapered with one prolate-spheroidal taper with time-bandwidth product $NW = 4$. Red curves are robust estimates of power from Chave's method; solid red circles indicate frequency resolution in the low-frequency portion; gray curves contain the 95% confidence intervals based on jackknifed error estimates.

correctly identified the large event in Figure 5a as one worth reporting, without false positives. As no such algorithm can be judged foolproof without extensive testing on much longer time series than we available so far, we shall refrain from publishing it here. However, it is available from the first author.

[37] The power spectral densities of the entire 600 s long data segments in the first column of Figure 5 are shown in the last column. The spectral signatures of these segments, which include identified seismic arrivals, vary from experiment to experiment. Those belonging to the first experiment include Figure 5a–5c, the second experiment yielded the data in Figure 5d, while the third experiment is represented by Figure 5e. The different hardware properties of the instrument as it was changed between experiments no doubt have influenced the spectral characteristics of the recorded time series, but exactly how is unclear.

[38] Figure 6 characterizes the instrument and ambient noise outside the intervals of positively detected (or even merely suspected) seismic signals. We obtained these curves by sectioning the entire time series shown in Figure 3 into hour-long overlapping sequences and then discarding those with known mechanical (e.g., pumping) or expected seismic energy. In particular, the detected segments shown in Figure 5 were removed. As in Figure 5 the power spectral analysis was performed on the uncorrected raw data without any scaling, thus the power scales between both figures can be compared without adjustment. As noted earlier the qualitative differences between the three experiments are very clear. We suspect the influence of hardware settings, especially in causing the curious increase in noise levels in the low-frequency portion of the third experiment shown in Figure 6c. Accounting for these differences and acknowledging potential instrumental problems, it is tempting to interpret the generally high power around 0.2–0.3 Hz, the notch around 0.1 Hz and the increasing power below this frequency as resulting from microseismic noise [*Webb and Cox*, 1986; *D'Spain et al.*, 1991; *Babcock et al.*, 1994; *Webb*, 1998]. However, rather than treating these spectra as "absolute" measurements of acoustic noise pressure, we shall use them for future reference to aid with subsequent design modifications. Most importantly, we shall deduce from Figures 5 and 6 that detecting teleseismic earthquakes with dominant periods around 0.5–1 Hz using the current MERMAID instrument remains challenging, but is not altogether impossible under sufficiently quiet oceanic conditions.

Figure 5. Seismic events detected at 700 m depth offshore San Diego, CA, during the recovered deployments of the MERMAID prototype float. Only the event in Figure 5a is teleseismic and thus suited for global tomography. Figure layout mimicks that of Figure 4, and analyses are conducted identically, with different settings where indicated. (first column) Filtered time domain data sections, in arbitrary scaled units, from the (a–c) November 2003, (d) September 2004, and (e) August 2007 experiments, aligned on the expected arrival time of the earthquakes' *P* wave predicted in the *iasp91* Earth model using United States Geological Survey (NEIC) PDE locations and the then last known location of the instrument. Labels show the 2-pole, 2-pass Butterworth filter passband (in Hz), the NEIC earthquake magnitude (mag) and depth (d) and its approximate epicentral distance (Δ) in angular degrees. (second column) Spectrograms from WOSA with 10 s Hann tapers with 87.5% overlap. (third column) Thresholded scalograms of the lifted CDF (2,4) transform. (fourth column) Spectral densities and 95% confidence intervals of the unscaled data, from WOSA with a $NW = 4$ prolate-spheroidal taper on 70% overlapping 500 s segments.

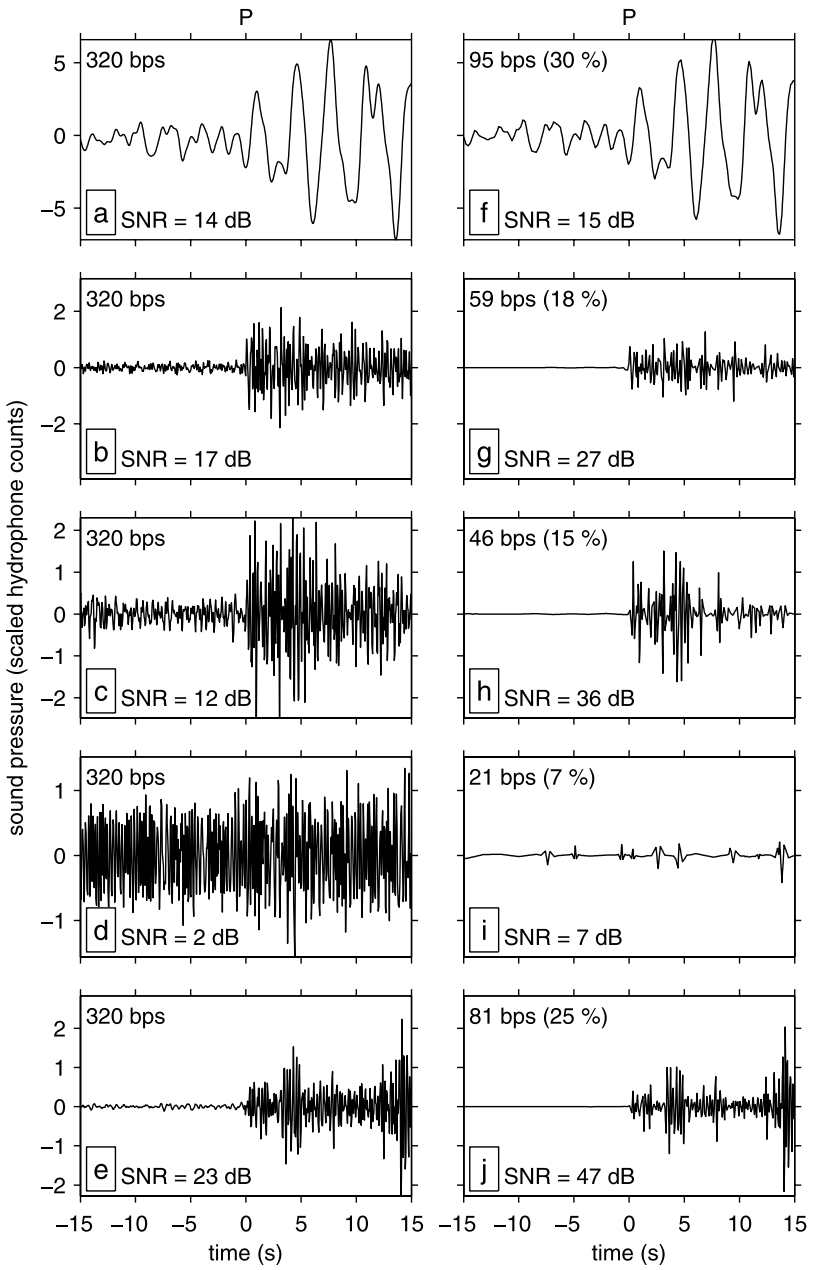

Figure 7. Zooms on the seismic arrivals of the detected segments shown in Figure 5. (left column) Figures 7a–7e contain 30 s segments of the data from the identically lettered panels in Figure 5, aligned by eye on the actual *P* wave arrival time. Also marked are the bit rate (bps), assuming 16-bit data nominally sampled at 20 Hz and the energy signal-to-noise ratio (SNR) determined by interpreting the first half of the segment shown to be noise and the second half as signal. (right column) Figures 7f–7j contain the corresponding wavelet-denoised segments, i.e., the waveforms reconstructed after thresholding of the CDF (2,4) wavelet coefficients of the seismograms in the left column, and the corresponding lower bit rates and enhanced signal-to-noise ratios.

[39] With Figure 7 we conclude this section with a more detailed look at the onset of the detected seismic phases. The lettering on Figures 7a–7e corresponds to the rows of Figure 5, and the filter settings between both figures are unchanged, but the time windows shown are now only 30 s long. This enables us to get a feel for the expected accuracy in determining arrival times from even a single MERMAID instrument. Moreover, we will use these sections to calculate the signal-to-noise ratio (SNR) of the incoming (filtered) arrivals. In contrast to Figure 5, we have now aligned the traces on the *P* arrival as identified by eye, and no longer on the arrival to the uncertain float location as expected in the *iasp91* model. In practice, this has meant shifting the center portions of the windows shown in Figures 5a–5e by −5, −13.4, −15, +20 and +4 s, respectively. We define the SNR here to be ten times the logarithm of the ratio of the mean of the squared signal halves (before and after the presumptive *P* arrival). This quantity is shown in the bottom

left corner of each panel. Those signals that our own STA/LTA and scalogram-based algorithms detected and differentiated (i.e. all signals but the one shown in Figure 5d–Figure 7) had a SNR exceeding 12 dB. This is encouragingly lower than the 16 dB advocated for detection by *Webb* [1998].

[40] The second column, Figures 7f–7j, shows the same waveforms reconstructed after soft thresholding of their wavelet transform. The denoising capabilities of this procedure are readily apparent to the naked eye and quantified by the corresponding increase in SNR. Both the detected teleseismic event in Figure 7a and the undetected local event in Figure 7d appear to have gained little from thresholding. The former barely registers an increase in SNR, presumably due to the long-period character of the noise in this particular record, which the thresholding of wavelet coefficients at coarseness scales $\leq$5 does not filter out. The latter remains not unequivocally detectable even in the denoised record.

[41] Thresholding does lower the number of coefficients needed to represent the signal of these recordings, which can be stored and transmitted in much compressed form, should the need arise. We calculate the data rate of the recordings for 16 bit sampling at 20 Hz before and after wavelet denoising. We assume that the wavelet coefficients have indeed been calculated using the fast integer-to-integer (rounded) lifting transform [*Sweldens*, 1996; *Calderbank et al.*, 1998], and that zeroed coefficients do not need encoding. Data rates are quoted in bits per second (bps) in the top left corner of each panel in Figure 7, and the compression achieved by denoising appears as a percentage comparing the records in the second column to the first. Without claiming that a reduction in bandwidth will ultimately be necessary once the final design of MERMAID includes an IRIDIUM satellite subscription, our examples show that compression factor rates up to 4:1 appear readily achievable, which is instructive in its own right.

6. Discussion: A Future for MERMAID

[42] The future of MERMAID will depend on the acquisition cost per useful *P* wave. We hesitate to put a dollar amount on an array of MERMAID devices, but, based on past experience, a conservative estimate is one third the cost of a state-of-the-art three-component ocean bottom seismometer (OBS). Deployment costs are expected to be one hundredth to one tenth of an OBS installation and recovery campaign. This leaves us to determine the likely number of usable events detected by a single MERMAID over the course of a typical campaign. No data on power consumption are as yet available, although it is clear that this will be the limiting factor. In oceanographic scenarios, such as the Argo project of global Conductivity-Temperature-Depth (CTD) profiling [*Dalton*, 2002; *Gould et al.*, 2004], where sensor demands and sampling rates are comparatively low, current batteries allow for 150 to 200 dive cycles [*Davis et al.*, 2001; *D'Asaro*, 2007]. Sampling 20 Hz seismic data and performing the necessary detection and discrimination routines will represent a multifold increase in power drainage, even with analog detection and efficient wavelet-based discrimination, but the precise numbers require the completion of longer-term tests.

[43] Five events were unequivocally detected in our 121 h of data from MERMAID. They ranged from the close and faint (magnitudes <3 and distances in the 1°–10° range) to the large and distant (a magnitude of 6 at a distance exceeding 45°). Pressure sensitivity is the crucial factor, as a 1 mm oscillation of the instrument in the water column produces a signal of about 10 Pa. Other noises also contribute, and the pressure induced by even a magnitude 6 earthquake at teleseismic distances is not expected to much exceed this value (see below). Thus in order to be able to define a ''region of detectability'' in the space of earthquake magnitude-epicentral distance, and from there to estimate the number of likely detections based on a global earthquake catalog, we must be able to put a sound pressure scale on all events missed and detected so far.

[44] To this end, we proceed following *Reid et al.* [1973], with some refinements. We calculate the ground motion amplitude induced by an earthquake of a given magnitude at a given distance, take into account the incidence angle by computing the ray parameter in the *iasp91* earth model, compute the transmission coefficient and take-off angle at the ocean floor, and thence the pressure variation expected in the water. This leads to a sound pressure perturbation due to an incoming *P* wave of

$$p = \rho_w \alpha \omega u_z(\phi)/\cos(\theta), \tag{1}$$

where ρ_w = 1000 kg m^{-3} is the water density; α = 5800 m s^{-1} is the P wave speed nearest the ocean floor; $\omega = 2\pi f$ is the angular frequency with f = 1 Hz the nominal frequency for ''large'' events with known body wave magnitude, and f = 5 Hz for ''small'' events with known local magnitude; θ is the angle with the vertical of the upcoming wave in the water; and $u_z(\phi)$ is the vertical component of ground motion for a wave that comes into the ocean bottom at an angle ϕ with the normal. The angles θ and ϕ are related by Snel's law; for the propagation speed in water we used α_w = 1500 m s^{-1}. We note that, due to the presence of the free surface, equation (1) needs to be amended by a factor $\sin(\omega z/\alpha_w)$ to describe the pressure sensitivity at a depth z below the surface [*Ewing et al.*, 1957; *Lewis and Dorman*, 1998]. While $z = 375/f$ is thus ideal theoretically, the best cruising depth also depends on the relative location with respect to the axis of the noisy SOFAR channel.

[45] This leaves the task of computing ground displacement, u, predicted from an earthquake catalog. We shall take a very simple approach and use the rule [*Shearer*, 1999; *Udias*, 2000]

$$u = 10^{m_l - 2.56 \log \Delta + 1.67}, \tag{2}$$

with the epicentral distance Δ given in km, for events whose local magnitude m_l is listed; the result is in micrometers (μm). When body wave magnitude m_b is known, we use instead

$$u = 10^{(m_b - Q(\Delta))}/f, \tag{3}$$

for a frequency of f = 1 Hz and $Q(\Delta)$ a distance-dependent correction factor, tabulated by *Bormann* [2002] (Table 6 on their Data Sheet 3.1), which ranges from about 6 to 7 for

shallow events (i.e. having a hypocenter less than 70 km deep, admittedly a clear oversimplification [*Veith and Clawson*, 1972; *Nolet et al.*, 1998]). The result again is in μm. Neither of these rules are expected to be very accurate [see, e.g., *Wu et al.*, 2006], but when consistently applied, they should permit a relative measure of detectability, which is to be calibrated by the actual data collected in situ.

[46] The results are shown in Figure 8. All 389 events whose pressure conversions were in principle detectable during one of the three MERMAID pilot experiments are plotted, with symbols varying between campaigns, in terms of their magnitude, epicentral distance, and sound pressure level. The latter is expressed in decibel (dB), $20 \times \log(p/p_{max})$, relative to the maximum computed acoustic pressure over the entire set. Not surprisingly pressure levels increase with event size and proximity to the sensor, as seen in Figure 8a. The detected events that were the subject of section 3 and Figures 5 and 7 are also marked by crosses. Alternative views through the three-dimensional space are shown in Figure 8b–8c. Figure 8b is perhaps the most instructive; it shows that the approximate loci of events at equal epicentral distance lie along lines with constant slope on a graph of logarithmic sound pressure versus earthquake magnitude. The five detected events all appear at the high end of the scale with sound pressure levels above −10 dB.

[47] We elected to show sound pressure on a relative scale due to the substantial uncertainties in converting reported earthquake magnitudes to absolute ground displacement at uninstrumented locations on the ocean floor, which could be one order of magnitude or more. Also ignored in our simple model, the intricacies involved in accurately predicting pressure from individual earthquakes, such as radiation patterns, site effects, and three-dimensional Earth structure, will lead to further variance in the first-order picture of Figure 8. However, it is encouraging that we seem to have recorded those earthquakes with the largest calculated pressure effects. Alas, in the distance-magnitude space of Figure 8a, the detected events appear to be at the edge of a region that must be defined more clearly than is possible on the basis of just 389 contemporaneous events.

[48] To better define the level surface of sound pressure in distance-magnitude space, we carried out an analysis identical to the one described above on all of 55,924 events found in the NEIC catalog for a period of two years starting 1 November 2003. The acoustic pressure variations across all hypocenter depths were predicted based purely on epicentral distance, ray parameter and arrival angle in the *iasp91* model, as well as the empirical scaling of magnitude to ground motion, and again separately considered at frequencies of 1 Hz for the body wave magnitudes and 5 Hz for the local events. The analysis yielded a well-defined surface that we interpolated and contoured. One such contour, at −8.5 dB (using the maximum acoustic pressure level of the set of only 389 events as reference), is plotted in Figure 8a. While it has a not unexpected irregular edge in

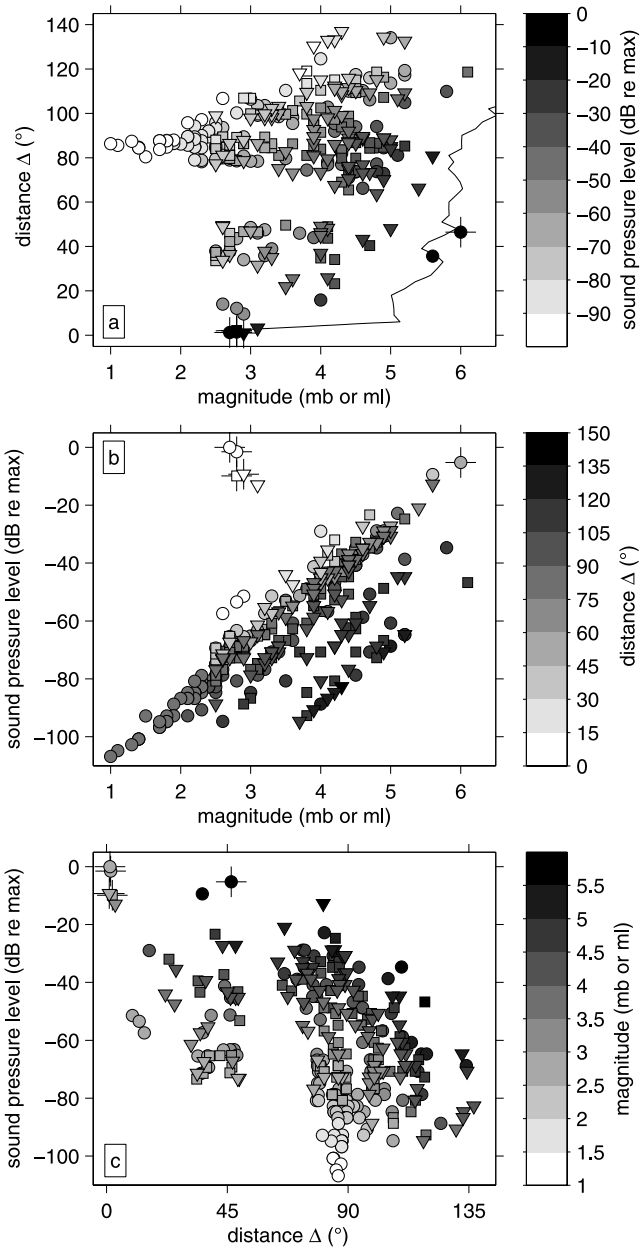

Figure 8. Three views through the space of earthquake magnitude, distance, and acoustic pressure for all 389 events in the NEIC catalog whose converted pressure waves were predicted to arrive within the three underwater data collection periods (the intervals shown in Figure 3) in November 2003 (circles), September 2004 (squares), and August 2007 (triangles). The detected events (whose details are shown in Figure 5) are also marked by crosses. The data shown are epicentral distance, body-wave (m_b) or local (m_l) catalog magnitude, and sound pressure at 1 Hz (for m_b) or 5 Hz (for m_l) predicted from empirical magnitude-to-ground displacement scaling, and ray parameters and transmission coefficients calculated in the *iasp91* Earth model. The jagged black line in Figure 8a, which is approximately linear on a logarithmic distance scale, separates the detected (to its right) from the nondetected (to its left) events in the distance-magnitude section and coincides with the −8.5 dB contour of sound pressure level (0 dB corresponds to the maximum acoustic pressure of the data shown in this graph) determined from a similar analysis of all 55,924 events with magnitude greater than 2, across all focal depths, in the NEIC catalog in a 2-year period starting 1 November 2003.

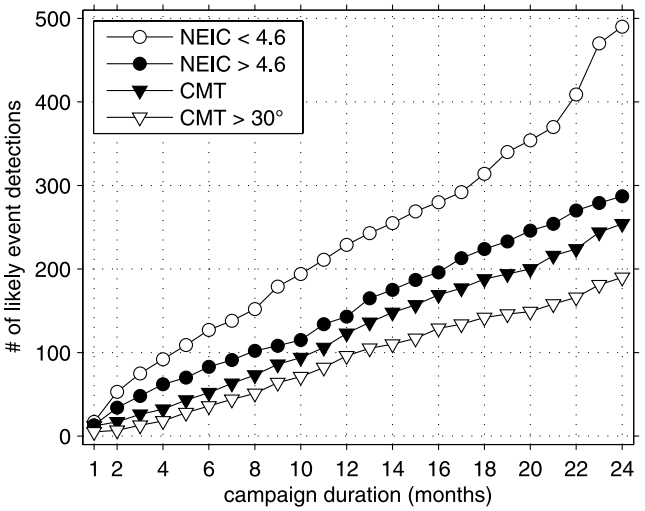

Figure 9. Likely numbers of event detections as a function of campaign duration (disregarding power limitations) with the current MERMAID prototype, based on the analysis presented in Figure 8. We used the boundary in magnitude-distance space shown in Figure 8a as a plausible indicator of subaqueous detectability, and distinguish between events reported over a 2-year window in the CMT and NEIC catalogs, subdividing the latter into those events larger and smaller than magnitude 4.6, the lowest magnitude on record in the CMT catalog, and the former by epicentral distance.

this linear distance scale, it approximately defines a straight line in function of logarithmic distance versus magnitude. We chose the level of −8.5 dB because of its clean demarcation of the 389 recordable events into the 384 that MERMAID missed and the 5 that she captured.

[49] More importantly, we shall adhere to this −8.5 dB pressure level contour in order to make an estimate of the number of events likely to be detected in the course of a campaign with MERMAID. We leave power issues aside for the moment and reiterate the important caveat that our experiments were conducted under relatively quiet ocean conditions. Thus while our estimates are not referenced to any particular location of the instrument, they will depend on local conditions. We added all the events in the two yearlong NEIC catalog that fell to the right of the curve plotted in Figure 8a, in function of increasing experiment duration, and proceeded identically for two years of data in the CMT catalog (www.globalcmt.org). The investigated portion of the CMT catalog had a lower magnitude cutoff of 4.6. We used this value to subdivide our results based on the NEIC catalog into those exceeding or falling below this threshold. The results are plotted in Figure 9 and show that an instrument of the MERMAID type has the required sensitivity to build, over time, an important database of global earthquakes recorded at teleseismic distances, sampling hitherto uncharted regions within the Earth. In addition, it is to be expected that MERMAID will contribute to the study of smaller regional earthquakes as well. For this, the onboard discrimination algorithm must be switched to accept rather than reject local earthquakes.

[50] As shown by *McCreery and Duennebier* [1993] and *Babcock et al.* [1994], among others, oceanographic and meteorological conditions play a great role in determining noise levels and thus teleseismic detection thresholds at a dominant period of 1 Hz in practical scenarios [e.g., *Slack et al.*, 1999; *Wilcock et al.*, 1999; *Fox et al.*, 2001]. Our interpretation is optimistic and will need to be validated by in situ experiments on a much longer timescale and at more than one depth with respect to the local axis of the SOFAR channel. Detecting teleseismic body wave arrivals at periods longer than the 1–2 s than we have been considering for our analysis might be relatively easier as far as oceanic noise is concerned (see Figure 6). In that case, however, we would need increased, and well-characterized, sound pressure sensitivity at the lowest frequencies. Furthermore, as long-period traveltimes are harder to measure absolutely due to the presence of reverberations [*Lewis and Dorman*, 1998], more precise relative determinations could be made by cross-correlation of waveforms from an array of nearby instruments, whose relative positions, however, would need to be known with great accuracy [*Hodgkiss and Anderson*, 1983; *Chen and Hodgkiss*, 1993].

7. Conclusions

[51] For global seismic tomography, the importance of deploying oceanic equipment is well known and cannot be overstated. We have developed a low-cost, free-floating, oceanic device called MERMAID (Mobile Earthquake Recording in Marine Areas by Independent Divers) to address the seismic coverage gap over oceanic areas, with the long-term objective of improving the resolution of global tomographic Earth models. The device consists of a hydrophone carried by a SOLO float, a popular platform in oceanography, with a custom-built data logging package. Over the course of three pilot experiments under oceanographically and meteorologically quiet conditions 120 h of data were collected at a depth of 700 m. These time series of acoustic pressure variations yielded positive identifications of five earthquakes across magnitude and distance ranges that suggest an upper bound on detections of about 100 tomographically useful teleseismic events per year. The next-generation MERMAID will operate completely autonomously, with built-in wavelet-based signal processing detection and discrimination software designed and tested on training data from moored hydrophones as well as on data obtained by the prototype in situ. Power limitations continue to be the driving force behind improvements to the basic instrument described in this paper, but our results show the great potential of MERMAID in completing catalogs of mantle phases over time with existing technology. This makes MERMAID the most cost-effective and versatile instrument for seismic applications.

[52] **Acknowledgments.** The MAR and EPR data are jointly provided by NOAA/PMEL Acoustics Project Office, Woods Hole Oceanographic Institution, and Lamont-Doherty Earth Observatory. We thank Del Bohnenstiehl, Bob Dziak, Joe Haxel, and Maya Tolstoy for help in accessing and interpreting them. We thank John Orcutt for assistance throughout the project and Bud Vincent for constructive comments on the manuscript. We are indebted to Del Bohnenstiehl, John Mutter, Pallavi Nuka, an anonymous reviewer and the associate editor for their help in editing and improving the manuscript, both stylistically and scientifically. Finally, we acknowledge

financial support from U.S. National Science Foundation grants EAR-0105387, EAR-0710860, and EAR-0236557, U.K. Natural Environmental Research Council grant NE/D521449/1, and Nuffield Foundation grant NAL/01087/G. All computer code is made available on www.frederik.net.

References

Aki, K. (1967), Scaling law of seismic spectrum, *J. Geophys. Res.*, *72*(4), 1217–1231.

Allen, R. V. (1978), Automatic earthquake recognition and timing from single traces, *Bull. Seismol. Soc. Am.*, *68*(5), 1521–1532.

Allen, R. V. (1982), Automatic phase pickers: Their present use and future prospects, *Bull. Seismol. Soc. Am.*, *72*(6), S225–S242.

Allen, R. M., and H. Kanamori (2003), The potential for earthquake early warning in Southern California, *Science*, *300*, 786–789, doi:10.1126/science.1080912.

Babcock, J. M., B. A. Kirkendall, and J. A. Orcutt (1994), Relationships between ocean bottom noise and the environment, *Bull. Seismol. Soc. Am.*, *84*(6), 1991–2007.

Bauer, E., and C. Staabs (1998), Statistical properties of global significant wave heights and their use for validation, *J. Geophys. Res.*, *103*(C1), 1153–1166.

Bohnenstiehl, D. R., M. Tolstoy, R. P. Dziak, C. G. Fox, and D. K. Smith (2002), Aftershock sequences in the mid-ocean ridge environment: An analysis using hydroacoustic data, *Tectonophysics*, *354*, 49–70, doi:10.1016/S0040-1951(02)00289-5.

Bormann, P. (Ed.) (2002), *New Manual of Seismological Observatory Practice*, 2nd ed., GeoForschungsZentrum, Potsdam, Germany.

Bradner, H. (1964), Seismic measurements on the ocean bottom, *Science*, *146*(3641), 208–216.

Bradner, H., and J. N. Brune (1974), Use of sonobuoys in determining hypocenters of aftershocks of February 21, 1973 Pt. Mugu earthquake, *Bull. Seismol. Soc. Am.*, *64*(1), 99–101.

Bradner, H., L. G. de Jerphanion, and R. Langlois (1970), Ocean microseism measurements with a neutral buoyancy free-floating midwater seismometer, *Bull. Seismol. Soc. Am.*, *60*, 1139–1150.

Butler, R., and C. Lomnitz (2002), Coupled seismoacoustic modes on the seafloor, *Geophys. Res. Lett.*, *29*(10), 1418, 10.1029/2002GL014722.

Calderbank, R., I. Daubechies, W. Sweldens, and B.-L. Yeo (1998), Wavelet transforms that map integers to integers, *Appl. Comput. Harmon. Anal.*, *5*(3), 332–369.

Campillo, M., and A. Paul (2003), Long-range correlations in the diffuse seismic coda, *Science*, *299*(5606), 547–549.

Chakraborty, A., and D. Okaya (1995), Frequency-time decomposition of seismic data using wavelet-based methods, *Geophysics*, *60*(6), 1906–1916.

Chave, A. D., D. J. Thomson, and M. E. Ander (1987), On the robust estimation of power spectra, coherences, and transfer functions, *J. Geophys. Res.*, *92*(B1), 633–648.

Chen, G. C., and W. S. Hodgkiss (1993), VLF source localization with a freely drifting acoustic sensor array, *IEEE J. Oceanic Eng.*, *18*(3), 209–223.

Cohen, A., I. Daubechies, and J. Feauveau (1992), Biorthogonal bases of compactly supported wavelets, *Comm. Pure Appl. Math.*, *45*, 485–560, doi:10.1002/cpa.3160450.

Cotaras, F. D., I. A. Fraser, and H. M. Merklinger (1988), Near-surface ocean ambient noise measurements at very low-frequencies, *J. Acoust. Soc. Am.*, *83*(4), 1345–1359.

Cox, C. S., and D. C. Jacobs (1989), Cartesian diver observations of double frequency pressure-fluctuations in the upper levels of the ocean, *Geophys. Res. Lett.*, *16*(8), 807–810.

Dahlen, F. A., S.-H. Hung, and G. Nolet (2000), Fréchet kernels for finite-frequency traveltimes—I. Theory, *Geophys. J. Int.*, *141*(1), 157–174.

Dalton, R. (2002), Oceanography: Voyage of the argonauts, *Nature*, *415*(6875), 954–955, doi:10.1038/415954a.

D'Asaro, E. A. (2007), Solar power for autonomous floats, *J. Atmos. Oceanogr. Technol.*, *24*(7), 1309–1314, doi:10.1175/JTECH2041.1.

Daubechies, I. (1990), The wavelet transform, time-frequency localization and signal analysis, *IEEE Trans. Inform. Theory*, *36*(5), 961–1005.

Daubechies, I. (1992), *Ten Lectures on Wavelets, CBMS-NSF Regional Conference Series in Applied Mathematics*, vol. 61, Society for Industrial and Applied Mathematics, Philadelphia, Penn.

Daubechies, I., and W. Sweldens (1998), Factoring wavelet transforms into lifting steps, *J. Fourier Anal. Appl.*, *4*(3), 247–269, doi:10.1007/BF02476026.

Davis, R. E. (2005), Intermediate-depth circulation of the Indian and South Pacific oceans measured by autonomous floats, *J. Phys. Oceanogr.*, *35*(5), 683–707.

Davis, R. E., J. T. Sherman, and J. Dufour (2001), Profiling ALACEs and other advances in autonomous subsurface floats, *J. Atmos. Oceanogr. Technol.*, *18*(6), 982–993.

Davis, R. E., D. C. Webb, L. A. Regier, and J. Dufour (1992), The Autonomous Lagrangian Circulation Explorer (ALACE), *J. Atmos. Oceanogr. Technol.*, *9*(3), 264–285.

de Groot-Hedlin, C. D. (2005), Estimation of the rupture length and velocity of the Great Sumatra earthquake of Dec 26, 2004 using hydroacoustic signals, *Geophys. Res. Lett.*, *32*, L11303, doi:10.1029/2005GL022695.

Donoho, D., and I. M. Johnstone (1994), Ideal spatial adaptation by wavelet shrinkage, *Biometrika*, *81*(3), 425–455.

D'Spain, G. L., W. S. Hodgkiss, and G. L. Edmonds (1991), The simultaneous measurement of infrasonic acoustic particle-velocity and acoustic pressure in the ocean by freely drifting Swallow floats, *IEEE J. Oceanic Eng.*, *16*(2), 195–207.

Duennebier, F. K., D. W. Harris, J. Jolly, J. Babinec, D. Copson, and K. Stiffel (2002), The Hawaii-2 observatory seismic system, *IEEE J. Oceanic Eng.*, *27*(2), 212–217.

Dziak, R. P., D. R. Bohnenstiehl, H. Matsumoto, C. G. Fox, D. K. Smith, M. Tolstoy, T.-K. Lau, J. H. Haxel, and M. J. Fowler (2004), *P*- and *T*-wave detection thresholds, *Pn* velocity estimate, and detection of lower mantle and core *P*-waves on ocean sound-channel hydrophones at the Mid-Atlantic Ridge, *Bull. Seismol. Soc. Am.*, *94*(2), 665–677.

Evans, J. R., and S. S. Allen (1983), A teleseism-specific detection algorithm for single short period traces, *Bull. Seismol. Soc. Am.*, *73*(4), 1173–1186.

Ewing, W. M., W. S. Jardetzky, and F. Press (1957), *Elastic Waves in Layered Media*, *International Series in the Earth Sciences*, McGraw-Hill, New York.

Forsyth, D. W., and the MELT Seismic Team (1998), Imaging the deep seismic structure beneath a mid-ocean ridge: The MELT experiment, *Science*, *280*(5367), 1215–1218, doi:10.1126/science.280.5367.1215.

Fox, C. G., R. P. Dziak, H. Matsumoto, and A. E. Schreiner (1993), Potential for monitoring low-level seismicity on the Juan-de-Fuca ridge using military hydrophone arrays, *Mar. Technol. Soc. J.*, *27*(4), 22–30.

Fox, C. G., H. Matsumoto, and T.-K. A. Lau (2001), Monitoring Pacific Ocean seismicity from an autonomous hydrophone array, *J. Geophys. Res.*, *106*(B3), 1347–1352.

Gendron, P., J. Ebel, and D. Manolakis (2000), Rapid joint detection and classification with wavelet bases via Bayes theorem, *Bull. Seismol. Soc. Am.*, *90*(3), 764–774.

Gledhill, K. R. (1985), An earthquake detector employing frequency domain techniques, *Bull. Seismol. Soc. Am.*, *75*(6), 1827–1835.

Goforth, T., and E. Herrin (1981), An automatic seismic signal detection algorithm based on the Walsh transform, *Bull. Seismol. Soc. Am.*, *71*(4), 1351–1360.

Gould, J., et al. (2004), Argo profiling floats bring new era of in situ ocean observations, *EOS Trans. AGU*, *85*(19), 185, doi:10.1029/2004EO190002.

Gray, L. M., and D. S. Greeley (1980), Source level model for propeller blade rate radiation for the world's merchant fleet, *J. Acoust. Soc. Am.*, *67*(2), 516–522.

Hodgkiss, W. S., and V. C. Anderson (1983), Acoustic positioning for an array of freely drifting infrasonic sensors, *IEEE J. Oceanic Eng.*, *8*(3), 116–119.

Ishii, M., and J. Tromp (1999), Normal-mode and free-air gravity constraints on lateral variations in velocity and density of Earth's mantle, *Science*, *285*, 1231–1236.

Isse, T., H. Shiobara, Y. Fukao, K. Mochizuki, T. Kanazawa, H. Sugioka, S. Kodaira, R. Hino, and D. Suetsugu (2004), Rayleigh wave phase velocity measurements across the Philippine Sea from a broad-band OBS array, *Geophys. J. Int.*, *158*(1), 257–266, doi:10.1111/j.1365-246X.2004.02322.x.

Jensen, A., and A. la Cour-Harbo (2001), *Ripples in Mathematics*, Sringer, Berlin.

Johnstone, I. M., and B. W. Silverman (1997), Wavelet threshold estimators for data with correlated noise, *J. R. Stat. Soc. Ser. B*, *59*(2), 319–351.

Joswig, M. (1990), Pattern recognition for earthquake detection, *Bull. Seismol. Soc. Am.*, *80*(1), 170–186.

Kebe, H.-W. (1981), Self-noise measurements using a moored sonobuoy with a suspended hydrophone, *Mar. Geophys. Res.*, *5*(2), 207–220.

Kumar, P., and E. Foufoula-Georgiou (1997), Wavelet analysis for geophysical applications, *Rev. Geophys.*, *35*(4), 385–412.

Laske, G., J. Phipps Morgan, and J. A. Orcutt (2007), The Hawaiian SWELL pilot experiment—Evidence for lithosphere rejuvenation from ocean bottom surface wave data, *Geol. Soc. Am. Spec. Pap.*, *430*, 209–233, doi:10.1130/2007.2430(11).

Lewis, B. T. R., and L. M. Dorman (1998), Recording teleseisms on the seafloor; an example from the Juan de Fuca plate, *Bull. Seismol. Soc. Am.*, *88*(1), 107–116.

Mallat, S. (1998), *A Wavelet Tour of Signal Processing*, Academic Press, San Diego, Calif.

McCreery, C. S., and F. K. Duennebier (1993), Correlation of deep ocean noise (0.4-30 Hz) with wind, and the Holu spectrum—A worldwide constant, *J. Acoust. Soc. Am.*, *93*(5), 2639–2648.

McDonald, M. A., and J. A. Hildebrand (1995), Blue and fin whales observed on a seafloor array in the Northeast Pacific, *J. Acoust. Soc. Am.*, *98*(2), 712–712.

Nishimura, C. E., and D. M. Conlon (1993), IUSS dual-use: Monitoring whales and earthquakes using SOSUS, *Mar. Technol. Soc. J.*, *27*(4), 13–21.

Nolet, G. (2008), *A Breviary for Seismic Tomography*, Cambridge Univ. Press, Cambridge, UK.

Nolet, G., S. Krueger, and R. M. Clouser (1998), Empirical determination of depth-distance corrections for m_b and m_w from Global Seismograph Network stations, *Geophys. Res. Lett.*, *25*(9), 1451–1454.

O'Hanlon, L. (2001), Seismic sleuths, *Nature*, *411*(6839), 734–736.

Park, Y.-G., K.-H. Oh, K.-I. Chang, and M.-S. Suk (2004), Intermediate level circulation of the southwestern part of the East/Japan Sea estimated from autonomous isobaric profiling floats, *Geophys. Res. Lett.*, *31*, L13213, doi:10.1029/2004GL020424.

Percival, D. B., and A. T. Walden (1993), *Spectral Analysis for Physical Applications, Multitaper and Conventional Univariate Techniques*, Cambridge Univ. Press, New York.

Poupinet, G., M. Pasquier, M. Vadell, and L. Martel (1989), A seismological platform transmitting via Meteosat, *Bull. Seismol. Soc. Am.*, *79*(5), 1651–1661.

Reid, I., M. Reichle, J. Brune, and H. Bradner (1973), Microearthquake studies using sonobuoys: Preliminary results from the Gulf of California, *Geophys. J. R. Astron. Soc.*, *34*(3), 365–379.

Rioul, O., and M. Vetterli (1991), Wavelets and signal processing, *IEEE Signal Process. Mag.*, *8*(4), 14–38.

Romanowicz, B. (1991), Seismic tomography of the Earth's mantle, *Annu. Rev. Earth. Planet. Sci.*, *19*, 77–99.

Romanowicz, B. (2003), Global mantle tomography: Progress status in the last 10 years, *Annu. Rev. Geophys. Space Phys.*, *31*, 303–328, doi:10.1146/annurev.earth.31.091602.113555.

Romanowicz, B. (2008), Using seismic waves to image Earth's structure, *Nature*, *451*, 266–268, doi:10.1038/nature06583.

Romanowicz, B., and D. Giardini (2001), The future of permanent seismic networks, *Science*, *293*(5537), 2000–2001, doi:10.1126/science.1061771.

Romanowicz, B., D. Stakes, D. Dolenc, D. Neuhauser, P. McGill, R. Urhammer, and T. Ramirez (2006), The Monterey Bay broadband ocean bottom seismic observatory, *Ann. Geophys.*, *49*(2-3), 607–623.

Shearer, P. M. (1999), *Introduction to Seismology*, Cambridge Univ. Press, Cambridge, UK.

Simons, F. J., B. D. E. Dando, and R. M. Allen (2006a), Automatic detection and rapid determination of earthquake magnitude by wavelet multiscale analysis of the primary arrival, *Earth Planet. Sci. Lett.*, *250*(1-2), 214–223, doi:10.1016/j.epsl.2006.07.039.

Simons, F. J., G. Nolet, J. M. Babcock, R. E. Davis, and J. A. Orcutt (2006b), A future for drifting seismic networks, *Eos Trans. AGU*, *87*(31), 305, doi:10.1029/2006EO310002.

Slack, P. D., C. G. Fox, and R. P. Dziak (1999), *P* wave detection thresholds, P_n velocity estimates, and *T* wave location uncertainty from oceanic hydrophones, *J. Geophys. Res.*, *104*(B6), 13,061–13,072.

Smith, D. K., M. Tolstoy, C. G. Fox, D. R. Bohnenstiehl, H. Matsumoto, and M. J. Fowler (2002), Hydroacoustic monitoring of seismicity at the slow spreading Mid-Atlantic Ridge, *Geophys. Res. Lett.*, *29*(11), 1518, doi:10.1029/2001GL013912.

Smith, D. K., R. P. Dziak, H. Matsumoto, C. G. Fox, and M. Tolstoy (2004), Autonomous hydrophone array monitors seismic activity at northern Mid-Atlantic Ridge, *Eos Trans. AGU*, *85*(1), 1–5, doi:10.1029/2004EO010001.

Smith, G. P., D. A. Wiens, K. M. Fischer, L. M. Dorman, S. C. Webb, and J. A. Hildebrand (2001), A complex pattern of mantle flow in the Lau backarc, *Science*, *292*(5517), 713–716, doi:10.1126/science.1058763.

Stafford, K. M., S. L. Nieukirk, and C. G. Fox (2001), Geographic and seasonal variation of blue whale calls in the North Pacific, *J. Cetacean Res. Manage.*, *3*(1), 65–76.

Stephen, R. A., F. N. Spiess, J. A. Collins, J. A. Hildebrand, J. A. Orcutt, K. R. Peal, F. L. Vernon, and F. B. Wooding (2003), Ocean Seismic Network Pilot Experiment, *Geochem. Geophys. Geosyst.*, *4*(10), 1092, doi:10.1029/2002GC000485.

Strang, G., and T. Nguyen (1997), *Wavelets and Filter Banks*, 2nd ed., Wellesley-Cambridge Press, Wellesley, Mass.

Swallow, J. C. (1955), A neutral-buoyancy float for measuring deep currents, *Deep-Sea Res.*, *3*(1), 74–81.

Sweldens, W. (1996), The lifting scheme: A custom-design construction of biorthogonal wavelets, *Appl. Comput. Harmon. Anal.*, *3*(2), 186–200.

Tibi, R., D. A. Wiens, H. Shiobara, H. Sugioka, and P. Shore (2006), Depth of the 660-km discontinuity near the Mariana slab from an array of ocean bottom seismographs, *Geophys. Res. Lett.*, *33*, L02313, doi:10.1029/2005GL024523.

Tolstoy, I., and M. Ewing (1950), The *T* phase of shallow-focus earthquakes, *Bull. Seismol. Soc. Am.*, *40*(1), 25–51.

Tolstoy, M., et al. (2006), A sea-floor spreading event captured by seismometers, *Science*, *314*(5807), 1920–1922, doi:10.1126/science.1133950.

Udías, A. (2000), *Principles of Seismology*, Cambridge Univ. Press, Cambridge, UK.

Veith, K. F., and G. E. Clawson (1972), Magnitude from short-period *P* data, *Bull. Seismol. Soc. Am.*, *62*(2), 435–452.

Webb, D. C., P. J. Simonetti, and C. P. Jones (2001), SLOCUM: An underwater glider propelled by environmental energy, *IEEE J. Oceanic Eng.*, *26*(4), 447–452.

Webb, S. C. (1988), Long-period acoustic and seismic measurements and ocean floor currents, *IEEE J. Oceanic Eng.*, *13*(4), 263–270.

Webb, S. C. (1998), Broadband seismology and noise under the ocean, *Rev. Geophys.*, *36*(1), 105–142.

Webb, S. C., and C. S. Cox (1986), Observations and modeling of seafloor microseisms, *J. Geophys. Res.*, *91*(B7), 7343–7358.

Wenz, G. M. (1962), Acoustic ambient noise in the ocean: Spectra and sources, *J. Acoust. Soc. Am.*, *34*(12).

Wilcock, W. S. D., S. C. Webb, and I. T. Bjarnason (1999), The effect of local wind on seismic noise near 1 Hz at the MELT site and in Iceland, *Bull. Seismol. Soc. Am.*, *89*(6), 1543–1557.

Willis, J. K., and L.-L. Fu (2008), Combining altimeter and subsurface float data to estimate the time-averaged circulation in the upper ocean, *J. Geophys. Res.*, *113*, C12017, doi:10.1029/2007JC004690.

Wu, Y.-M., H.-Y. Yen, L. Zhao, B.-S. Huang, and W.-T. Liang (2006), Magnitude determination using initial *P*-waves: A single-station approach, *Geophys. Res. Lett.*, *33*, L05306, doi:10.1029/2005GL025395.

Xie, J., and J. Zhu (2008), Estimation of the surface and mid-depth currents from Argo floats in the Pacific and error analysis, *J. Mar. Syst.*, *73*, 61–75, doi:10.1016/j.jmarsys.2007.09.001.

Zhao, D., Y. Xu, D. A. Wiens, L. Dorman, J. Hildebrand, and S. Webb (1997), Depth extent of the Lau backarc spreading center and its relationship to subduction processes, *Science*, *278*, 254–257, doi:10.1126/science.278.5336.254.

J. M. Babcock and P. Georgief, Institute of Geophysics and Planetary Physics, Ocean Bottom Seismometry Laboratory, Scripps Institution of Oceanography, Munk Laboratory, La Jolla, CA 92093-0225, USA.

R. E. Davis and L. A. Regier, Physical Oceanography Research Division, Instrument Development Group, Scripps Institution of Oceanography, Nierenberg Hall, La Jolla, CA 92093-0230, USA.

G. Nolet and F. J. Simons, Geosciences Department, Princeton University, Guyot Hall 321B, Princeton, NJ 08544, USA. (fjsimons@alum.mit.edu)